

The gluon condensation in hadron collisions

Wei Zhu^{a*}, Qihui Chen^b, Zhiyi Cui^a and Jianhong Ruan^a

^aDepartment of Physics, East China Normal University, Shanghai 200241, P.R. China

^bSchool of Physical Science and Technology Southwest Jiaotong University,
Chengdu 610031, P.R. China

Abstract

Gluons may converge to a stable state at a critical momentum in hadrons. This gluon condensation is predicted by a nonlinear QCD evolution equation. We review the understanding of the gluon condensation and present a clear physical picture that produces the gluon condensation from the colour glass condensate. We summarize the applications of the GC effect in the $p - p(A)$ collisions and predict that the $p - Pb$ and $Pb - Pb$ collisions at the LHC are close to the energy region of the gluon condensation. We warn that for the next generation of hadron colliders with the increasing of the collision energy, the extremely strong gamma-rays will be emitted in a narrow space of the accelerator due to the gluon condensation effect. Such artificial mini gamma-ray bursts in the laboratory may damage the detectors.

keywords: Gluon condensation; Antishadowing effect; Next generation of LHC

*Corresponding author, E-mail: wzhu@phy.ecnu.edu.cn

1 Introduction

Hadron in infinite momentum frame is consisted of partons (i.e., quarks and gluons). Gluons distribute mainly in the small x range (x is the Bjorken variable) and they dominate the high energy hadronic processes. The parton distribution functions are evolved according to the evolution equations based on perturbative QCD (pQCD) in the standard model. For example, the gluon distribution functions satisfy the Dokshitzer-Gribov-Lipatov-Altarelli-Parisi (DGLAP) equation in a broad kinematic range, its elemental amplitude is shown in Fig. 1a, where the correlations among initial partons are neglected [1]. Obviously, these correlations should be considered when the gluon density becomes large in very small x region, where the wave functions of the initial partons begin to overlap. Adding the initial gluons to the elemental amplitude of the DGLAP equation, one can get a series of modified elemental amplitudes in Figs. 1(b)-1(d), corresponding to the Balitsky-Fadin-Kuraev-Lipatov (BFKL) [2], Gribov-Levin-Ryskin-Mueller-Qiu -Zhu-Ruan-Shen (GLR-MQ-ZRS) [3,4] and Zhu, Shen, Ruan (ZSR) [5] equations, respectively. For convenience, we use the names of authors to mark the different evolution equations. According to the standard quantum field theory, a complete evolution equation should include the contributions of all possible Feynman diagrams for energy-momentum conservation and infrared (IR) safety. Works [4,5] used the time ordered perturbative theory (TOPT) to derive the evolution equations in Fig. 1. Interestingly, one of the resulting evolution equation (ZSR) predicts that the gluons in hadron may converge at a critical momentum (Fig. 3). This is the gluon condensation (GC).

The GC is displayed in the numerical solution of an approximate evolution equation. A question is that the GC does exactly exist in the nature? or is it just an approximate solution of the equation, once the approach is improved, will the GC disappear? This work attempts to answer the above question in the following two steps.

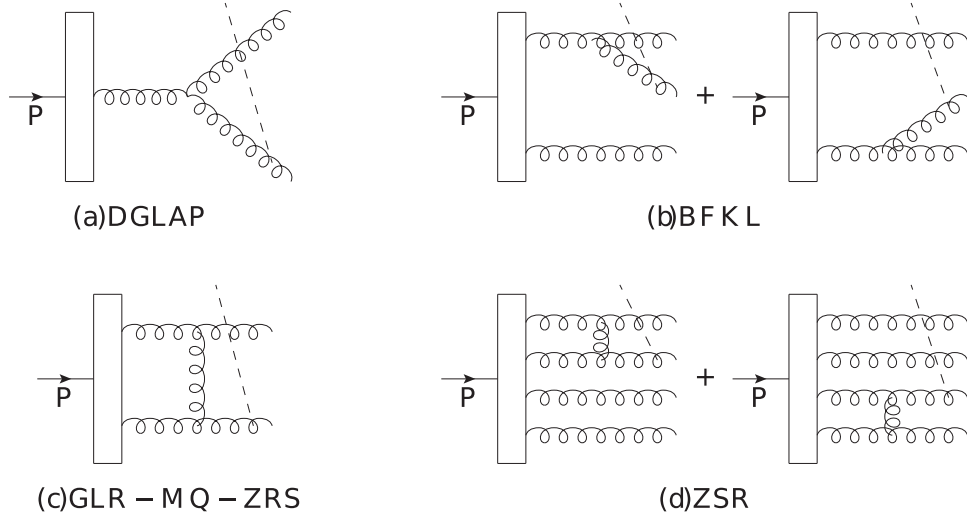


Figure 1: The corrections of the initial gluons to an elemental amplitude of the DGLAP equation (a) [1] and they lead to (b) the BFKL equation [2], (c) the GLR-MQ-ZRS equation [3-4] and (d) the ZSR evolution equation [5], respectively. The dashed line is a virtual current which probes gluons.

(1) We briefly review the GC-theory in Sec. 2, where we track the formation processes of the GC through Figs. 4 and 5. We noticed that the transverse momenta of the splitting and fusing gluons in hadrons at high energy processes are randomly changed. It leads to the so-called Lipatov-singularity [2]. This infrared singularity should be regularized by summing all relating Feynman diagrams according to the standard quantum field theory, after which, we can obtain Eq. (2.1), where both the linear and nonlinear parts have the regularized Lipatov-singularities. The nonlinear part in Eq. (2.1) converts the weak jumps on the gluon distributions into the strong chaotic oscillations. The chaotic oscillation generates the strong antishadowing effect, and the later leads to the GC. Thus, we show a more clear physical picture of the GC, which is quantitatively described by a delta-like function with the undetermined GC-critic momentum (x_c, k_c) .

(2) Then we turned to discuss the applications of the GC effect in Sec. 3. The GC should induce significant effects in the proton collisions if gluons with the GC-critic momentum enter the measuring energy region. Unfortunately, the value of (x_c, k_c) can not

been entirely determined in the theory since it relates to the unknown input conditions and high order modifications. We have not directly observed the GC-effects at the Large Hadron Collider (LHC). Therefore, the GC effect was used to analyse the astrophysical observations in [6-9], since the proton energy may be accelerated to cause the GC-effect in the hadronic collisions. Although the astrophysical phenomena relate to many complex factors, the GC effect as a general physical effect should be shown in the astronomical observation phenomenon. Specifically, cosmic gamma-rays can be generated in $p + p \rightarrow \pi^0 \rightarrow 2\gamma$. The sharp peak in the momentum distribution of gluons caused by the GC effect in Fig. 3 can suddenly increase the cross section in the hadron-hadron collisions, and results in a typical broken power law in the gamma-ray energy spectra, where the broken energy E_π^{GC} is determined by the critical momentum. After a brief summary we discuss the GC-threshold in the LHC energy range. We find that the interaction energies in the $p - Pb$ and $Pb - Pb$ collisions in LHC are close to the GC-energy region. Note that the cross section of pion production in the hadronic colliders can be increased by several orders of magnitude due to the GC effect, and about half of the proton kinetic energy converted to the photons of energy $E_\gamma = m_\pi/2$ with an extra intensity in a narrow space at the moment of collision. Therefore, we issue a warning for the next accelerator plans since such unexpected intense gamma rays in the laboratory may damage the detectors. Finally, the discussions and summary are given in Sec. 4, where we explain why the Balitsky-Kovchegov (BK) [10] does not have the GC solution. We also show the self-consistence among the popular QCD evolution equations.

2 The GC effect in the ZSR equation

The ZSR equation at the cylindrically symmetric approximation reads [5]

$$\begin{aligned}
& -x \frac{\partial F(x, k_{\perp}^2)}{\partial x} \\
& = \frac{3\alpha_s k_{\perp}^2}{\pi} \int_{k_0^2}^{\infty} \frac{dk'_{\perp}{}^2}{k'_{\perp}{}^2} \left\{ \frac{F(x, k'_{\perp}{}^2) - F(x, k_{\perp}^2)}{|k'_{\perp}{}^2 - k_{\perp}^2|} + \frac{F(x, k_{\perp}^2)}{\sqrt{k_{\perp}^4 + 4k'_{\perp}{}^4}} \right\} \\
& - \frac{81}{16} \frac{\alpha_s^2}{\pi R_N^2} \int_{k_0^2}^{\infty} \frac{dk'_{\perp}{}^2}{k'_{\perp}{}^2} \left\{ \frac{k_{\perp}^2 F^2(x, k'_{\perp}{}^2) - k'_{\perp}{}^2 F^2(x, k_{\perp}^2)}{k'_{\perp}{}^2 |k'_{\perp}{}^2 - k_{\perp}^2|} + \frac{F^2(x, k_{\perp}^2)}{\sqrt{k_{\perp}^4 + 4k'_{\perp}{}^4}} \right\}, \quad (2.1)
\end{aligned}$$

where F is the unintegrated gluon distribution and the linear part describes the contributions of the BFKL evolution. We used $F(x/2, k_{\perp}^2) \simeq F(x, k_{\perp}^2)$ near the saturation scale; the value of $R_N = 4 \text{ GeV}^{-1}$ is fixed by fitting the available experimental data of the proton structure functions.

We take two saturated inputs to evolve Eq. (2.1) starting from $x_0 = 4 \times 10^{-5}$. They are the Golec-Biernat and Wusthoff (GBW) model [11]

$$F_{GBW}(x_0, k_{\perp}^2) = \frac{3\sigma_0}{4\pi^2 \bar{\alpha}_s} R_0^2(x) k_{\perp}^4 \exp(-R_0^2(x) k_{\perp}^2), \quad (2.2)$$

where $\sigma_0 = 29.12 \text{ mb}$, $R_0(x) = 1/Q_s$, $Q_s = 1 \text{ GeV}$, $\bar{\alpha}_s = 0.2$, and the Kharzeev-Levin (KL) model [12]

$$F_{KL}(x_0, k_{\perp}^2) = \begin{cases} f_0 k_{\perp}^2 & \text{if } k_{\perp}^2 < Q_s^2 \\ f_0 Q_s^2 & \text{if } k_{\perp}^2 > Q_s^2, \end{cases} \quad (2.3)$$

where $f_0 = 10$. These two inputs are plotted in Fig.2, they describe the so called colour glass condensate (CGC) [13]. Note that in the calculations we take $F(x, k_{\perp}^2) = 0$ if $F(x, k_{\perp}^2) < 0$ since $F(x, k_{\perp}^2) \geq 0$ according to the definition of the gluon distribution.

The solutions of $F(x, k_{\perp}^2)$ in three-dimensional representation are given in Fig. 3, they show that gluons in the proton are converged at a critical momentum (x_c, k_c^2). In order

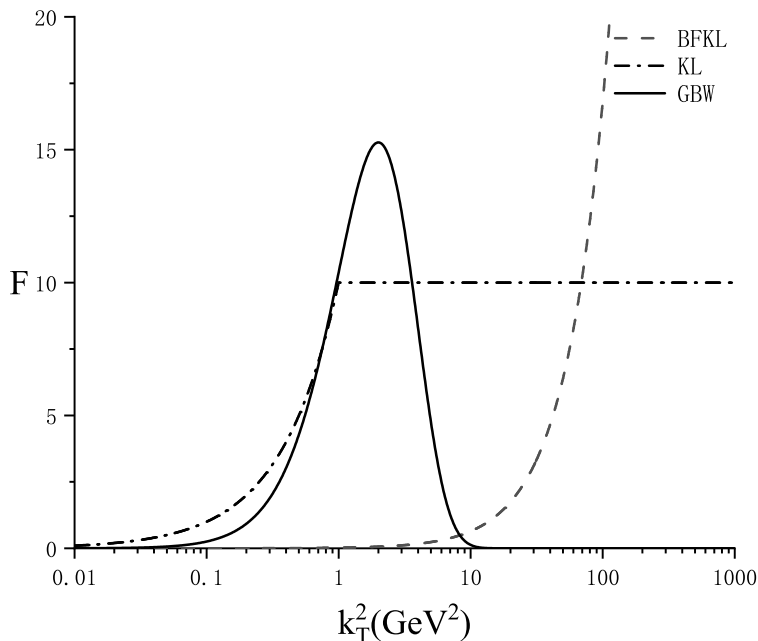


Figure 2: The GBW-, KL- and BFKL-inputs.

to expose its origin, we study the structure of Eq. (2.1). An important character of the BFKL dynamics is that the tracks of gluon motion on the transverse momentum k_{\perp} -plane are randomly distributed in the evolution. One can find that the variable k'_{\perp} may cross over k_{\perp} and generates the IR-divergences both in the linear and nonlinear kernels as shown in Eq. (2.1). However, any physical processes must be IR-safe. The most used nonlinear modifications to the BFKL equation take the way to avoid the IR-divergences, while these IR-divergences are canceled by using the TOPT cutting rule in works [4,5].

We draw the integrated function $R(x_0, k_{\perp}^2, k'_{\perp}{}^2) \sim k'_{\perp}{}^2$ of Eq. (2.1) at four different values of k_T^2 using two inputs (2.2) and (2.3) in Fig. 4. For comparison, a similar figure is also drawn but evolved by the linear BFKL equation with a normal BFKL-input [14]

$$F_{BFKL}(x_0, k_{\perp}^2) = \beta \sqrt{k_{\perp}^2} \frac{x_0^{-\lambda_{BFKL}}}{\sqrt{\ln(1/x_0)}} \exp\left(-\frac{\ln^2(k_{\perp}^2/k_s^2)}{2\lambda'' \ln(1/x_0)}\right), \quad (2.4)$$

where $\lambda_{BFKL} = 12\overline{\alpha}_s/(\pi \ln 2)$, $\lambda'' = 32\overline{\alpha}_s$, $\beta = 0.01$ and $k_s^2 = 1 \text{ GeV}^2$. One can find a

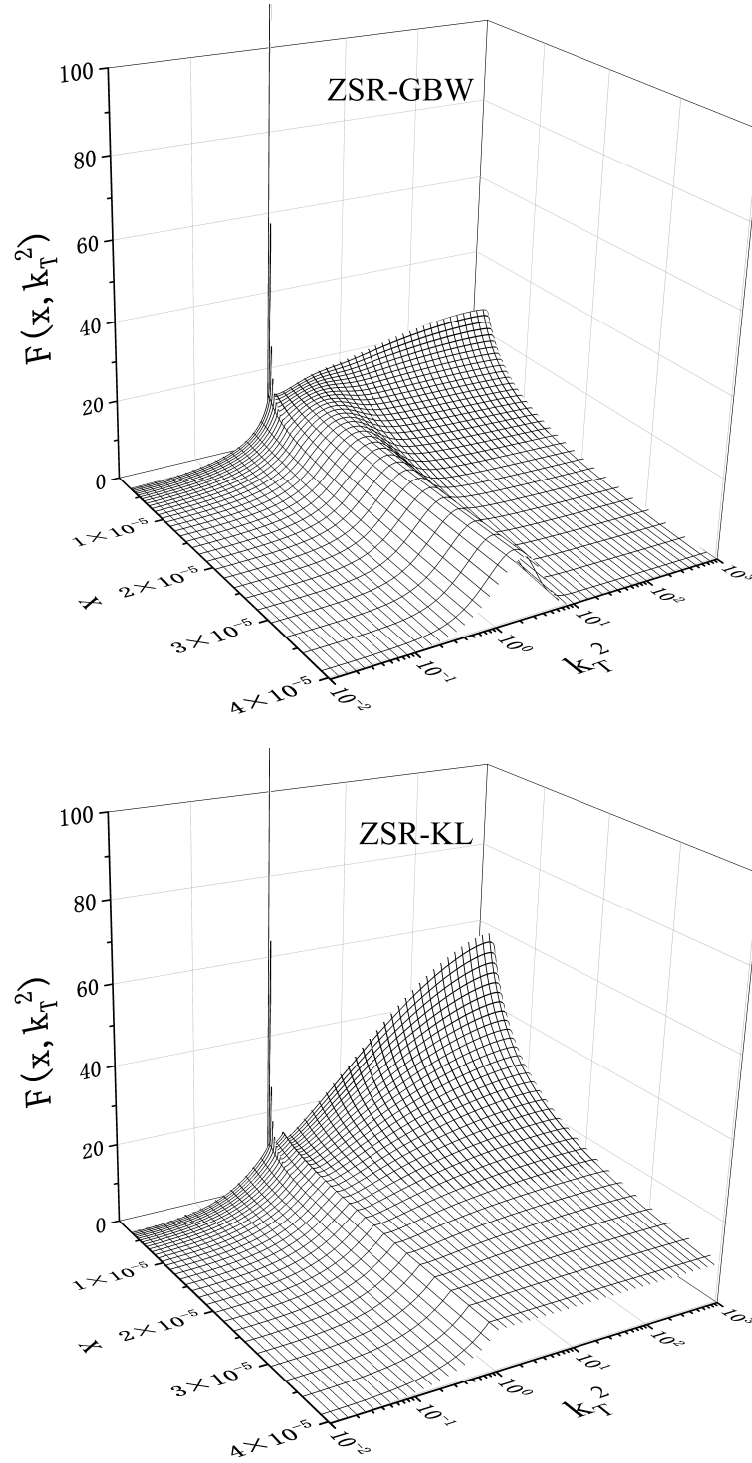


Figure 3: The solutions of Eq. (2.1) with the GBW- and KL-inputs, where the Runge-Kutta method is used.

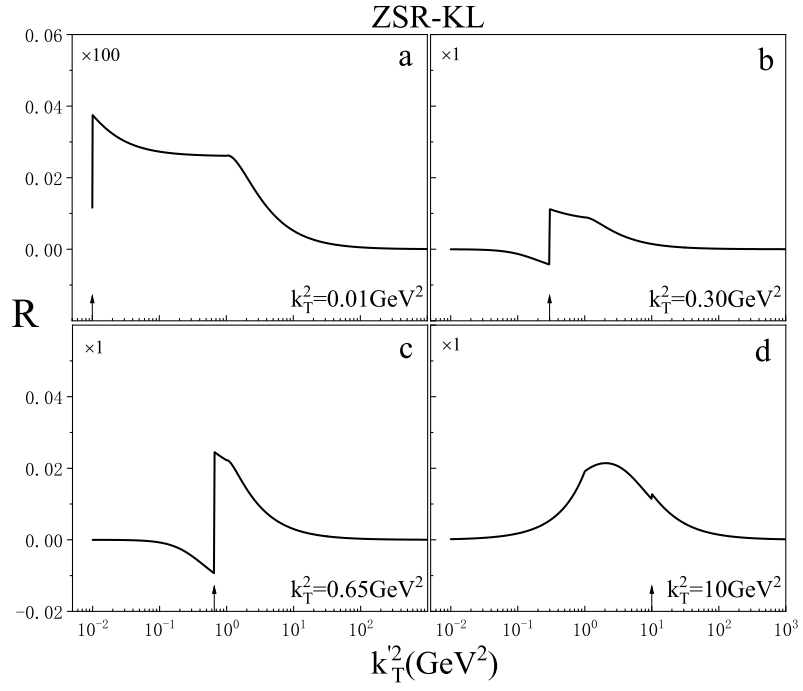
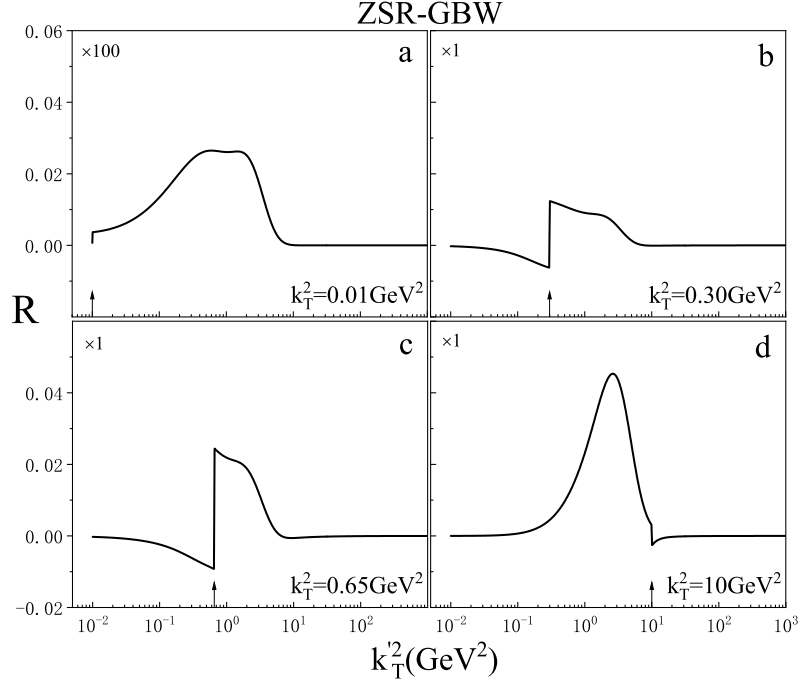
Table 1: The relations of the GC-critic momentum k_c with the nonlinear corrections.

Input	$k_c^2(\text{GeV}^2)$		
	nonlinear term $\times 0.5$	nonlinear term $\times (0.9\sim 1.4)$	nonlinear term $\times 5.0$
BFKL	0.0295	0.6531	0.6531
KL	0.0178	0.6531	1.000
GBW	0.0129	0.6531	0.933

common feature of the results: having jumps at $k_{\perp}'^2 = k_{\perp}^2$. It is the direct result of the Lipatov-singularity. After integral, these jumps generate a series of weak perturbations to the gluon distribution $F(x, k_{\perp}^2)$. The above perturbations are independent in the linear BFKL equation and their effects are negligibly small. In this case the solutions are almost smooth curves in the k_{\perp}^2 -dependence. However, the special nonlinear terms in Eq. (2.1) may occur the coupling among random perturbations and generates chaos. A standard criterion of chaos is that the system has the positive Lyapunov exponent, which indicates a strong sensitivity to small changes in the initial conditions. The Lyapunov exponents of the gluon distributions in Eq. (2.1) with the inputs Eqs. (2.2) and (2.3) are presented in Fig. 5. The positive Lyapunov exponent of the solutions of Eq. (2.1) is a strong evidence for the chaotic solution.

The critical momentum k_c^2 relates to the strength of the nonlinear terms of the QCD evolution equation. In order to verify this property, we multiply the nonlinear terms in Eq. (2.1) by a parameter A . Then we calculate the GC-critical momentum k_c using different values of A . The results in Table 1 show that the value of the critical momentum k_c in a certain range is determined by the structure of the evolution equations. Using this result we can predict the nuclear target dependence of the GC effect in the $p - A$ or $A - A$ collisions since the nonlinear terms of Eq. (2.1) are A -dependent. A is the mass number of a nucleus.

For comparison, we discuss the BK equation [10], which is generally considered as the



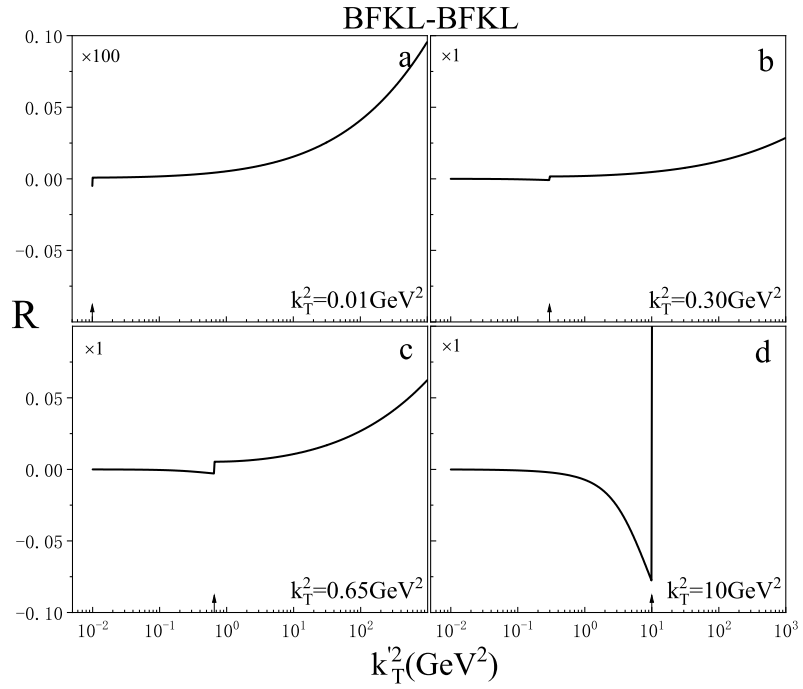


Figure 4: The transverse momentum dependence of the integrated function R in different evolution equations, where we use the GBW- and KL-inputs in Eq. (2.1) and the BFKL-input in the BFKL equation. One can find the jump structure, which will arise the chaotic solutions in Eq. (2.1).

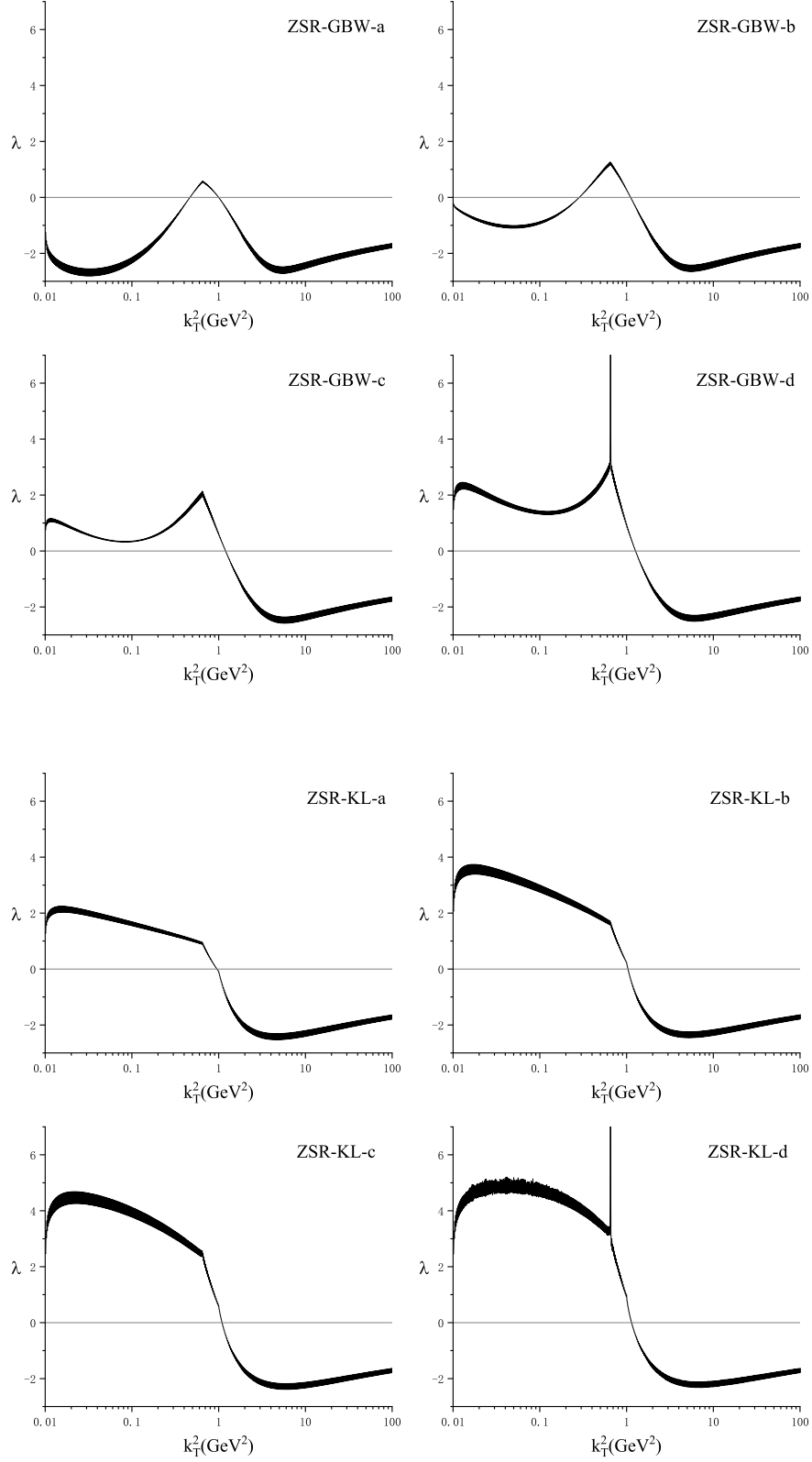


Figure 5: The Lyapunov exponents of the chaotic solutions in Eq. (2.1) using the GBW and KL inputs. The standard program of the Lyapunov exponents see Ref. [5].

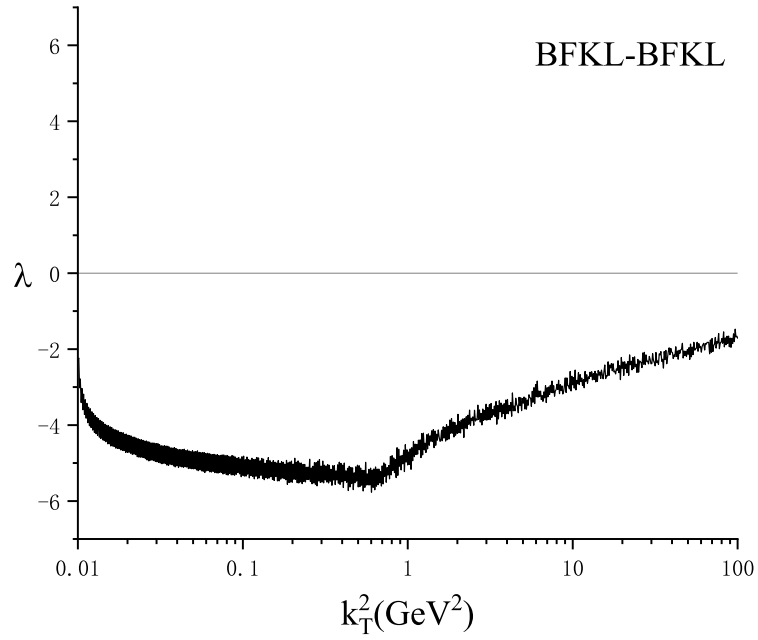
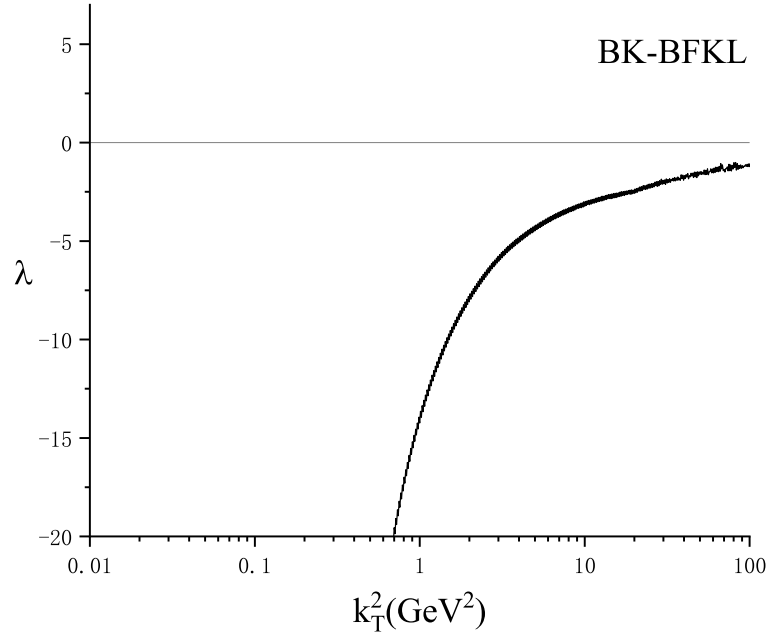


Figure 6: The Lyapunov exponents of the BK and BFKL equations using the BFKL-input.

typical nonlinear corrections to the BFKL equation at the leading order approximation.

The BK equation can be written in the full momentum space as [15,16]

$$\begin{aligned}
& -x \frac{\partial F(x, k_{\perp})}{\partial x} \\
& = \frac{\alpha_s N_c}{2\pi^2} \int d^2 k'_{\perp} \frac{k_{\perp}^2}{(k_{\perp} - k'_{\perp})^2 k_{\perp}^2} 2F(x, k'_{\perp}) - \frac{\alpha_s N_c}{2\pi^2} F(x, k_{\perp}) \int d^2 k'^2_{\perp} \frac{k_{\perp}^2}{(k_{\perp} - k'_{\perp})^2 k_{\perp}^2} \\
& \quad - \frac{18\alpha_s^2}{\pi R_N^2} \frac{N_c^2}{N_c^2 - 1} \frac{1}{k_{\perp}^2} F^2(x, k_{\perp}^2), \tag{2.5}
\end{aligned}$$

or taking the cylindrically symmetric approximation

$$\begin{aligned}
& -x \frac{\partial F(x, k_{\perp}^2)}{\partial x} \\
& = \frac{3\alpha_s k_{\perp}^2}{\pi} \int_{k'^2_{\perp}}^{\infty} \frac{dk'^2_{\perp}}{k'^2_{\perp}} \left\{ \frac{F(x, k'^2_{\perp}) - F(x, k_{\perp}^2)}{|k'^2_{\perp} - k_{\perp}^2|} + \frac{F(x, k_{\perp}^2)}{\sqrt{k_{\perp}^4 + 4k'^4_{\perp}}} \right\} - \frac{81}{4} \frac{\alpha_s^2}{\pi R_N^2} \frac{1}{k_{\perp}^2} F^2(x, k_{\perp}^2). \tag{2.6}
\end{aligned}$$

We find that both the BK and BFKL equations don't have the chaotic solutions since their Lyapunov exponents are negative (see Fig. 6).

With only the chaotic effect it cannot produce the GC solutions in Eq. (2.1). The TOPT regularized nonlinear kernel plays its second important role for converting the chaotic vibration into the strong shadowing and antishadowing effects, the later eventually forms the GC. Let us illustrate them. In Eq. (2.1) we have

$$\left[\frac{k_{\perp}^2 F^2(x, k'^2_{\perp})}{k'^2_{\perp} |k'^2_{\perp} - k_{\perp}^2|} - \frac{k'^2_{\perp} F^2(x, k_{\perp}^2)}{k_{\perp}^2 |k'^2_{\perp} - k_{\perp}^2|} \right]_{k'^2_{\perp} \sim k_{\perp}^2} \sim \frac{d}{dk'^2_{\perp}} \left[\frac{k_{\perp}^2}{k'^2_{\perp}} F^2(x, k'^2_{\perp}) \right]_{k'^2_{\perp} \sim k_{\perp}^2}. \tag{2.7}$$

Once chaos is produced, the fast oscillations of the gluon density will generate both the negative and positive nonlinear corrections to the increment $\Delta F(x, k_{\perp}^2)$ through derivative operations. Usually we call the negative or positive corrections to the nonlinear evolution equations as the shadowing or antishadowing effects. The former gradually suppresses the grownup of the gluon density since F^2 is also suppressed, while the later is a positive feedback process and it increases rapidly due to it is proportional to the increasing F^2 .

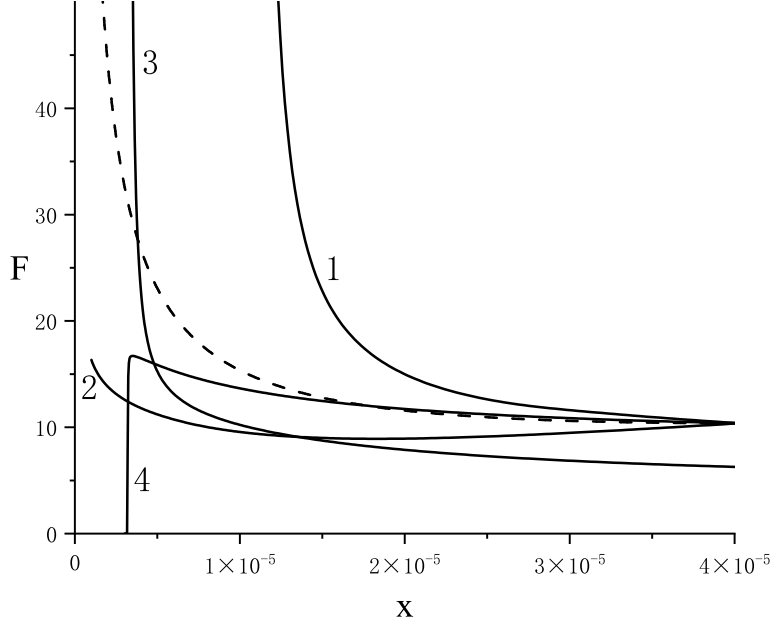


Figure 7: The net antishadowing effect (curve 1) and net shadowing effect (curve 2). Dashed curve is a solution of the linear BFKL equation. A pair of curves 3 and 4 are the solutions of Eq (2.1), where the shadowing and antishadowing are correlated by momentum conversion and they lead to the GC.

Let us consider Fig. 7, which presents the gluon distributions when the nonlinear terms in Eq. (2.1) take positive absolute values (curve 1), negative absolute values (curve 2) and zero value (dashed curve), they corresponding to the pure antishadowing effect, the pure shadowing effect and the linear BFKL evolution, respectively. One can find that the pure shadowing effect gradually suppresses the increasing gluon distribution, while the pure antishadowing leads to a fast divergence of the gluon density.

Note that the above examples show the isolate shadowing and antishadowing effects. In fact, the shadowing and antishadowing are correlated due to the local momentum conservation. Although Eq. (2.1) works at the small- x range and it does not describe the total momentum conservation, the local momentum conservation is still valid at every QCD vertex. The TOPT cutting rule in the derivation of Eq. (2.1) emphasises to sum all possible Feynman diagrams including real and virtual processes at the same order

approximation, as they naturally hold the local momentum conservation [5]. It leads to the correlation between the negative shadowing effect and the positive antishadowing effect, since these two effects origin from virtual and real diagrams, respectively. Thus, a strong antishadowing effect in Eq. (2.1) *must* be accompanied by the disappearance of the shadowed gluons due to the local momentum conservation as shown by a pair of curves 3 and 4 in Fig. 7. A similar example for the correlation of shadowing and antishadowing appears in a modified DGLAP equation [4], where the antishadowing effect is weaker than the shadowing effect since the integral range is restricted and the net shadowing effect dominates the process. The restriction of the resulting antishadowing effect has been confirmed by the observed EMC effect [17]. Thus, we do not need to design a mysterious mechanism to condense the gluons, the momentum conservation plus the net antishadowing effect in Eq. (2.1) may realize the GC.

Therefore, the GC is the combined effect of chaos and antishadowing in Eq. (2.1), which forms a GC-chain: the potential perturbation arises chaotic oscillations in the BFKL dynamics →generating the positive antishadowing corrections→converting the shadowed gluons to the gluons with the critical momentum (x_c, k_c) . Therefore, the gluon condensation is a natural consequence of random evolution of gluons at very high energy hadronic processes.

The unintegrated gluon distribution $F(x, k_\perp^2)$ of a bound nucleon in the nucleus A satisfies the following evolution equation

$$\begin{aligned}
& -x \frac{\partial F(x, k_\perp^2)}{\partial x} \\
& \simeq \frac{3\alpha_s k_\perp^2}{\pi} \int_{k_{\perp, \min}^2}^{\infty} \frac{dk_\perp'^2}{k_\perp'^2} \left\{ \frac{F(x, k_\perp'^2) - F(x, k_\perp^2)}{|k_\perp'^2 - k_\perp^2|} + \frac{F(x, k_\perp^2)}{\sqrt{k_\perp^4 + 4k_\perp'^4}} \right\} \\
& - \frac{81}{16} \frac{\alpha_s^2 A^{1/3}}{\pi R_N^2} \int_{k_{\perp, \min}^2}^{\infty} \frac{dk_\perp'^2}{k_\perp'^2} \left\{ \frac{k_\perp^2 F^2(x, k_\perp'^2) - k_\perp'^2 F^2(x, k_\perp^2)}{k_\perp'^2 |k_\perp'^2 - k_\perp^2|} + \frac{F^2(x, k_\perp^2)}{\sqrt{k_\perp^4 + 4k_\perp'^4}} \right\}. \quad (2.8)
\end{aligned}$$

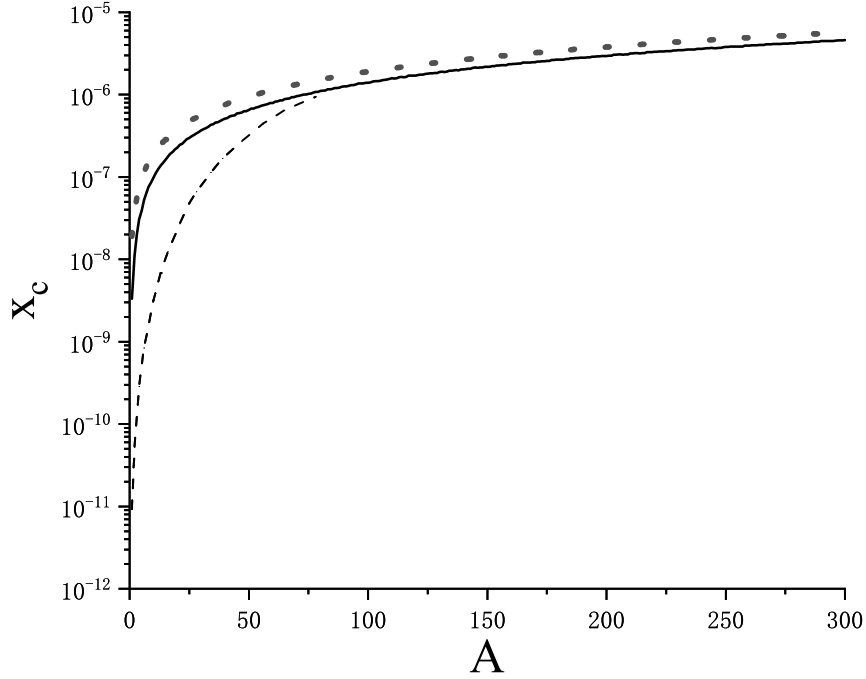


Figure 8: Predicted critic momentum x_c (solid curve) in different nuclear target. The point curve is $x_A = 1.9 \times 10^{-8}A$. The dashed curve is the possible modified x_c due to Eq. (3.16).

We take the K-L model in a nucleus A as the input of Eq. (2.8) at x_A

$$F(x_A, k_{\perp}^2) = \begin{cases} f_0 k_{\perp}^2 & \text{if } k_{\perp}^2 \leq Q_{A,s}^2 \\ f_0 Q_{A,s}^2 & \text{if } k_{\perp}^2 > Q_{A,s}^2 \end{cases}, \quad (2.9)$$

where $Q_{A,s}^2 = Q_s^2 A^{1/3}$, $Q_s = 1 \text{ GeV}$ is the saturation scale of a free nucleon [18].

Generally, the bigger the nucleus, the earlier Eq. (2.8) works. The GC-effect originates from the chaotic solution of Eq. (2.8). Once a most robust chaos is created, it will dominate the whole process of the condensation, no matter the event occurs whether in the longitudinal ($\sim A^{1/3}$) or horizontal ($\sim A^{2/3}$) area of the nucleus. Therefore, the starting point of evolution in Eq.(2.8) is proportional to the volume of a nucleus rather than its longitudinal scale, i.e., we take $x_A = x_p A$, x_p is the starting point of the Eq. (2.8) in a free nucleon. We use the input Eq. (2.9) and $x_p \equiv 1.9 \times 10^{-8}$ to calculate the relation $(x_c, k_c) \sim A$. The results are drawn in Figs. 8 and 9. We will use them to discuss

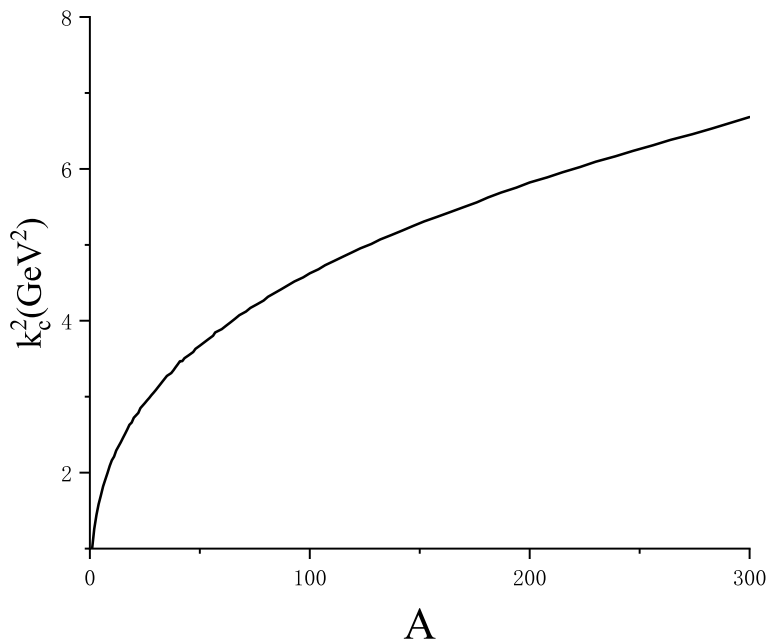


Figure 9: Predicted critic momentum k_c^2 in different nuclear targets.

the GC effect in hadron collisions in the following sections.

3 The GC-effect in the planning hadron collides beyond the LHC energies

We abstract some formulas for the applications of the GC effect in high energy hadron-hadron collisions and the detailed derivations can be found in works [6-9]. According to QCD, the yield of secondary particles at the high energy $p - p$ collision relates to the number of excited gluons, which participate in the multi-interactions. The number of pion will rapidly grow when a lot of gluons enter the interaction range due to the GC effect. Without concrete calculations, one can image that this will form an excess phenomenon in the cosmic-ray spectra. We focus on the central rapidity region, where the multi-hadrons (mainly pions) are produced due to the excited gluons. This process contains two steps

$$p + p \rightarrow \text{gluons (or gluons and quark - antiquark pairs)} \rightarrow n_\pi, \quad (3.1)$$

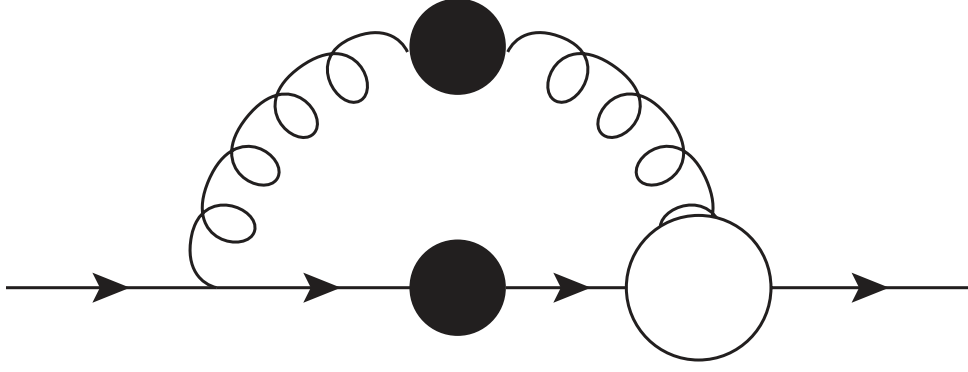


Figure 10: The self-energy diagram of obtaining effective constituent quark mass. Works [19] use it to explain the formation of pion mass. Empty circle is the DS vertex and black spots indicate the nonperturbative propagators, which contain the multi-parton components.

n_π is the multiplicity of the secondary pions.

Let us deeply understand the hadronization processes in the QCD-view. Based on the Dyson-Schwinger (DS) equation, the recent research by Roberts, et al., shows that the effective quark mass in hadron might be dynamically generated due to the gluon nonlinearities [19]. In this mechanism the nonperturbative gluon propagator is constructed by a lot of partons (i.e., gluons and sea quarks, note that the later is originated from gluons) in the hadron infinite momentum frame. A massless quark has got a small current quark mass through the Higgs mechanism and it further acquires the effective mass through the nonperturbative gluon propagator in the QCD self-energy diagram (Fig. 10). These "dressed" quarks are called as the constituent quarks. Now we compare the gluon distributions of the gluon condensate and the glasma. At the same collision energy \sqrt{s} , the gluon condensate has abundant gluons to greatly generate the number of the constituent quarks and increase the number n_π , i.e., $n_{\pi,GC} \gg n_{\pi,Glasma}$. On the other hand, we have $1/2\sqrt{s} \geq n_\pi m_\pi$ due to the restriction of the energy conservation. As a limit, we image that almost all available energy of the collision at the center-of-mass system is used to create pions.

Combining the relativistic invariant and energy conservation, one straightly writes [6,7]

$$(2m_p^2 + 2E_p m_p)^{1/2} = E_{p1}^* + E_{p2}^* + n_\pi m_\pi, \quad (3.2)$$

$$E_p + m_p = m_p \gamma_1 + m_p \gamma_2 + n_\pi m_\pi \gamma, \quad (3.3)$$

where E_{pi}^* is the energy of leading proton at the center-of-mass system, γ_i is the corresponding Lorentz factor. We can easily get the solutions of $n_\pi(E_p, E_\pi)$ in the $p-p$ collision

$$\ln n_\pi = 0.5 \ln E_p + a, \quad \ln n_\pi = \ln E_\pi + b, \quad (3.4)$$

where $E_\pi \in [E_\pi^{GC}, E_\pi^{max}]$. The parameters

$$a \equiv 0.5 \ln(2m_p) - \ln m_\pi + \ln 1/2, \quad (3.5)$$

and

$$b \equiv \ln(2m_p) - 2 \ln m_\pi + \ln 1/2. \quad (3.6)$$

These equations give the one-to-one relation among n_π , E_p and E_π^{GC} . Equation (3.4) gives the following special relation

$$E_p = e^{-2(a-b)} E_\pi^2 = \frac{2m_p}{m_\pi^2} E_\pi^2, \quad (3.7)$$

The upper limit $E_\pi^{max} = 14(E_\pi^{GC})^2$ (in the GeV-unit) if the charged particles can be accelerated continuously. However the actual E_π cannot reach such high limit because the restriction of acceleration mechanism. Therefore, we use a smaller cut-energy E_π^{cut} to replace E_π^{max} . E_π^{cut} relates to the accelerator mechanism and $E_\pi^{cut} \gg E_\pi^{GC}$. According to

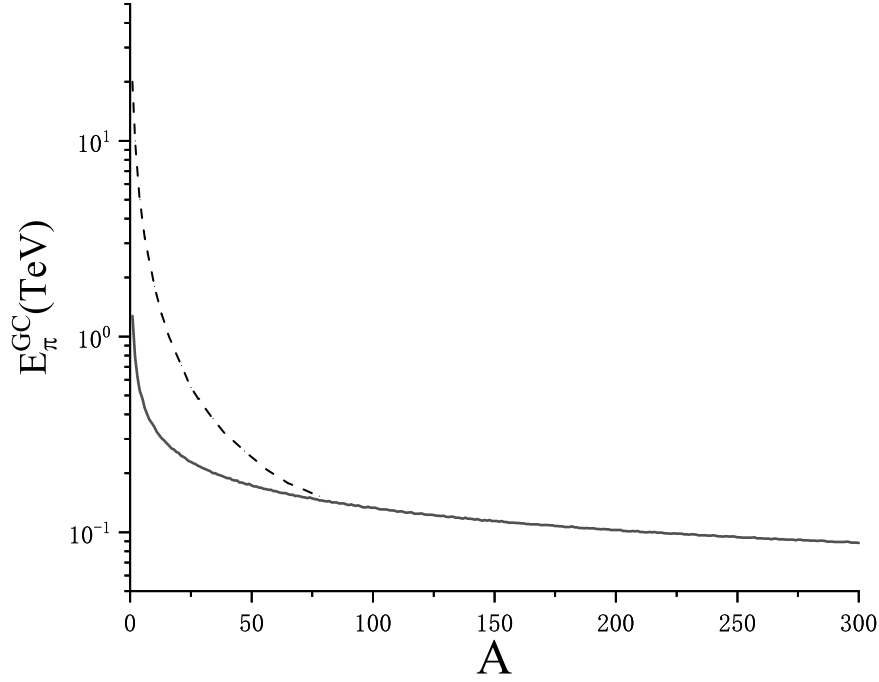


Figure 11: The predicted GC-threshold E_{π}^{GC} in the $p - A$ (or $A - A$) collisions (solid curve), which are obtained by Eq. (3.8) and the data of Figs. 8 and 9. The dashed curve is the possible modified GC-threshold E_{π}^{GC} due to the corrections of Eq. (3.8).

the numerical simulation, E_{π}^{cut} is required at least one order of magnitude greater than E_{π}^{GC} , i.e., $E_{\pi}^{cut} \geq 10E_{\pi}^{GC}$. E_{π}^{GC} and (x_c, k_c) have the following relation [6,7]

$$E_{\pi}^{GC} = \exp \left(0.5 \ln \frac{k_c^2}{2m_p x_c} + a - b \right) = \frac{m_{\pi}}{2m_p} \frac{k_c}{\sqrt{x_c}}. \quad (3.8)$$

Using this equation, one can predict the GC-threshold in Fig. 11. We find that the distribution of E_{π}^{GC} can be roughly divided into three ranges: (i) $E_{\pi}^{GC} \approx 100 \text{ GeV}$ for intermediate and heavy nuclei ($A > 100$), (ii) E_{π}^{GC} quickly increases for light nuclei ($A < 20$) and (iii) the area between them ($20 < A < 100$).

The contributions of proton and nucleus in the $p - A$ collisions dominate the rapidity distribution on the two sides of rapidity space, respectively. Note that the GC effect begins work when the gluons with x_A takes the first to participate the $A' - A$ collisions if $A > A'$, and enhances the total cross section of the collisions, therefore, we have

$E_{\pi}^{GC}(p - A) \simeq E_{\pi}^{GC}(A - A)$, although the GC-signal strength of the former is half weaker than the latter.

As we have known, the GC effect causes a big excess in the cross section of hadron collisions at center-of-mass energy $\sqrt{s^{GC}}$. In Tab. 2 we give these thresholds using Eqs. (3.7), (3.8) and the modified curve is shown in Fig. 11. For example, we take $E_{\pi}^{GC}(p - p) = 20$ TeV, thus, $E_{pp}^{GC} = 100 \times (2 \times 10^4)^2$ GeV = 4×10^{10} GeV and $\sqrt{s_{pp}^{GC}} = \sqrt{2m_p E_{pp}^{GC}} = 3 \times 10^2$ TeV. To observe the GC effect in the $p - p$ collision, one needs $E_{\pi}^{cut} \geq 10E_{\pi}^{GC}$, which requires $\sqrt{s_{pp}^{cut}} \geq 3 \times 10^3$ TeV. The maximum energies of the $p - p$ collision at the LHC is $\sqrt{s_{pp}} = 13$ TeV $\ll 3 \times 10^3$ TeV. Obviously, we can not record any GC-signals from the $p - p$ collision in the recent LHC.

Now we consider the the $p - Pb$ and $Pb - Pb$ collisions at the LHC, their maximum energies are 8.16 TeV and 5.02 TeV, respectively. Referring to Fig. 11, we take $E_{\pi}^{GC}(Pb - Pb) = 100$ GeV for them. The results are presented in Tab. 2. The energy region where the GC-signal appears is $\sqrt{s_{pPb}^{cut}} > 10$ TeV. Although the energies of these collisions in the LHC are already close to the GC-thresholds, it is still necessary to further increase the collision energy.

We emphasize that the GC effect may efficiently convert the kinetic energy of the parent protons into a large number of secondary particles. In fact, the multiplicity of mini gluon-jets in the hadronic collisions with the GC effect is about $10^3 - 10^4$ times larger than that without the GC model [5]. Besides, there is a highest gluon-pion conversion rate in the GC model. Thus, about half of the kinetic energy of protons are converted to the large numbers of photons with energy $E_{\gamma} = m_{\pi}/2$ in the center of mass (CM) frame in the $Pb - Pb$ collision. Such monochrome gamma-rays have extra high strength in a narrow space, and may damage the detectors in the laboratory.

We noticed that the Auger collaboration indirectly used the cosmic ray data at the

Table 2: The predicted center-of-mass energy $\sqrt{s_{pA}^{cut}}$ appearing the GC effect and the relating quantities in different hadronic collisions (in the GeV-unit).

Collisions	E_{π}^{GC}	E_{pA}^{GC}	$\sqrt{S_{pA}^{GC}}$	E_{π}^{cut}	E_{pA}^{cut}	$\sqrt{S_{pA}^{cut}}$
p-p	2×10^4	4×10^{10}	3×10^5	2×10^5	4×10^{12}	3×10^6
p-atm	$> 10^3$	$> 10^8$	$> 10^4$	$> 10^4$	$> 10^{10}$	$> 10^5$
p-Pb or Pb-Pb	10^2	10^6	10^3	10^3	10^8	10^4

top of the atmosphere and found that pA cross section at $\sqrt{s} \sim 100 \text{ TeV}$ is the normal value $\sim 567 \text{ mb}$ with no big increment [21]. According to Fig. 12 we guess that the GC-threshold $E_{\pi}^{GC}(p-atm) > 1 \text{ TeV}$ for light nuclei at the top of atmosphere. which implies $\sqrt{s_{p-atm}^{GC}} > 10 \text{ TeV}$, and $\sqrt{s_{p-atm}^{cut}} > 100 \text{ TeV}$. This result means that the observed energy by Auger collaboration at $\sqrt{s} = 100 \text{ TeV}$ is close to the lower-limit of the GC-effect range if the above mentioned indirect estimations are correct.

The more direct method of probing the GC effect in the laboratory is the Electron Ion Collider (EIC) [22] and the Large Hadron electron Collider (LHeC) [23]. The designed collision energy of upcoming EIC(US) is $\sqrt{s_{eA}} \simeq 140 \text{ GeV}$, which is in the CGC range ($x > 10^{-5}, Q^2 > 1 \text{ GeV}^2$). According to our estimation in Fig.8, the range of the GC effect is ($x_c \simeq 10^{-6}, k_c^2 \simeq 5 \text{ GeV}^2$), which exceeds the range of the EIC(US). However, the center-of-mass energy of the proposed Large Hadron electron Collider (LHeC) $\sqrt{s_{eA}} \sim 1 \text{ TeV}$ will be able to cover a very low x -range: $x \sim 10^{-6}$ at $Q^2 > 1 \text{ GeV}^2$ in eA collisions, where we may record the GC-signal.

Since the huge number of gluons are condensed in a critical momentum (x_c, k_c) , it should greatly increase the hadron cross section and release strong gamma-rays. We warn that further increase of the hadron collision energies in the next LHC plans may lead to unexpected intense gamma-rays in the accelerator, they look like the artificial mini GRBs and may damage the detectors

4 Discussions

(1) The evolution of the BFKL dynamics may become nonperturbative near the singular range mentioned above. Fortunately, both the lattice simulations and the nonperturbative dynamics of the QCD show that the effective strong coupling constant is restricted by $\alpha_s/\pi \leq B$ (B is a constant) [24].

(2) The equation (2.1) is based on the leading order approximation, where the higher order corrections are neglected. An important question is: will the chaos effects disappear in the evolution equation after considering higher order corrections? Works [5] have discussed this problem and we abstract some conclusions as follows. The GC effect origins from the singular nonlinear evolution kernel and local momentum conservation, they are general structure at the leading $\ln(1/x)$ -resummation. The multi-singular structure from higher order corrections should be cancelled by the contributions of the virtual Feynman diagrams at a same order level. The resulting nonlinear evolution equation is still keeping the conditions of existing GC. Although the higher order QCD corrections may change the value of k_c , however, the simple form of the GC solution contains only a few parameters (x_c, k_c) and they can be determined by the experimental data.

(3) The BK equation is generally considered as a typical nonlinear correction to the BFKL equation at the $LL(1/x)$ approximation and it is the most widely used small x evolution in the community. Why the BK equation doesn't have the chaotic solution? We try to answer this question. The BK equation is usually written by using the scattering amplitude $N(x_\perp, x)$ in the transverse coordinator space

$$\begin{aligned}
& -x \frac{\partial N(x_\perp, x)}{\partial x} \\
& = \frac{\alpha_s N_c}{2\pi^2} \int d^2 x'_\perp \frac{x_\perp^2}{x_\perp^2 (x_\perp - x'_\perp)^2} [N(x'_\perp, x) + N(x_\perp - x'_\perp, x) - N(x_\perp, x) \\
& \quad - N(x'_\perp, x) N(x_\perp - x'_\perp, x)].
\end{aligned} \tag{4.1}$$

The linear part corresponds to the BFKL evolution equation, while the nonlinear evolution kernel is regularized by the connecting amplitude $N(x'_\perp, x)N(x_\perp - x'_\perp, x)$ in the dipole splitting model to avoid the Lipatov-singularity. In order to illustrate the physical meaning of this regularization method, we use

$$N(x, k_{\perp}) = \int \frac{d^2 x_{\perp}}{2\pi} \exp(-ik_{\perp} \cdot x_{\perp}) \frac{N(x_{\perp}, x)}{x_{\perp}^2}, \quad (4.2)$$

to rewrite the BK equation in the transverse momentum space

$$\begin{aligned} & -x \frac{\partial N(x, k_{\perp}^2)}{\partial x} \\ &= \frac{3\alpha_s}{\pi} \int_{k'^2_{\perp}}^{\infty} \frac{dk'^2_{\perp}}{k'^2_{\perp}} \left\{ \frac{k'^2_{\perp} N(x, k'^2_{\perp}) - k_{\perp}^2 N(x, k_{\perp}^2)}{|k'^2_{\perp} - k_{\perp}^2|} + \frac{k_{\perp}^2 N(x, k_{\perp}^2)}{\sqrt{k_{\perp}^4 + 4k'^4_{\perp}}} \right\} - \frac{3\alpha_s}{\pi} N^2(x, k_{\perp}^2). \end{aligned} \quad (4.3)$$

If we define

$$N(x, k_{\perp}) \equiv \frac{27\alpha_s}{16k_{\perp}^2 R_N^2} F(x, k_{\perp}), \quad (4.4)$$

one can obtain Eq. (2.6) for the unintegrated gluon distribution $F(x, k_{\perp})$.

Let us to expose a relation between the ZSR and BK equations. The Lipatov-singularity in the nonlinear evolution kernel is arisen by the crossed diagrams of two different amplitudes in Fig. 1d and they imply the random evolution in the transverse momentum space. A simple, but unreasonable way for avoiding the singularity is to remove these crossed diagrams. In this case, one can find that Fig. 1d reduces to Fig. 1c. The latter is the contributions of the gluon fusion to the DGLAP evolution equation at the *DLL*-approximation, i.e.,

$$Q^2 \frac{\partial G(x, Q^2)}{\partial Q^2} = -\frac{36\alpha_s^2}{8Q^2 R_N^2} \frac{N_c^2}{N_c^2 - 1} \int \frac{dx'}{x'} G^2(x', Q^2), \quad (4.5)$$

where the transverse momenta of gluons are strongly ordered [3,4]. Note that the relation between gluon distribution $G(x, Q^2)$ and unintegrated gluon distribution $F(x, k_{\perp}^2)$ is

$$G(x, Q^2) \equiv \int_{k_{\perp, min}^2}^{Q^2} \frac{dk_{\perp}^2}{k_{\perp}^2} F(x, k_{\perp}^2). \quad (4.6)$$

We use $F(x, k_{\perp}^2)$ to replace $G(x, Q^2)$. From Eq.(5.5) we have

$$\Delta G(x, Q^2) = -18\alpha_s^2 \frac{N_c^2}{N_c^2 - 1} \int_{Q_{min}^2}^{Q^2} \frac{dk_{\perp}^2}{k_{\perp}^2} \int \frac{dx'}{x'} F^{(2)}(x', k_{\perp}^2), \quad (4.7)$$

or

$$\Delta F(x, k_{\perp}^2) = Q^2 \frac{\partial \Delta G(x, Q^2)}{\partial Q^2} \Big|_{Q^2=k_{\perp}^2} = -\frac{18\alpha_s^2}{\pi k_{\perp}^2 R_N^2} \frac{N_c^2}{N_c^2 - 1} \int \frac{dx'}{x'} F^2(x', k_{\perp}^2), \quad (4.8)$$

and

$$-x \frac{\partial F(x, k_{\perp}^2)}{\partial x} = -\frac{18\alpha_s^2}{\pi k_{\perp}^2 R_N^2} \frac{N_c^2}{N_c^2 - 1} F^2(x, k_{\perp}^2), \quad (4.9)$$

Where we define

$$F^{(2)}(x, k_{\perp}^2) \equiv \frac{1}{\pi^2 R_N^2} F^2(x, k_{\perp}^2). \quad (4.10)$$

Combining Eq. (4.9) with the linear BFKL equation, we can obtain the BK equation (2.6).

This example exposes a fact: the nonlinear part of the BK equation neglects the contributions of the random evolution of gluons on the transverse space. Therefore, the BK equation losses the GC-source since it avoids the Lipatov-singularity in the nonlinear kernel by using a dipole model. Thus, the BK equation and its general form [13] have not the GC solution.

Interestingly, we show the following evolution of the QCD evolution equations with increasing gluon densities:

The DGLAP equation ($|a|^2$) [Violation of unitarity]

\rightarrow *The BFKL equation ($|b|^2$) [Violation of unitarity]*

\rightarrow *The GLR – MQ – ZRS equation ($|a|^2 + |c|^2$) [Shadowing and antishadowing]*

→ *The BK equation* ($|a|^2 + |c|^2$) [*Saturation*]

→ *The ZSR equation* ($|b|^2 + |d|^2$) [*Gluon condensation*],

where the brackets mark the amplitude structure using Fig. 1, and square brackets contain the predicted effects. This picture reflects the self-consistence of the evolution equations including Eq. (2.1).

In summary, we present our new understanding of the GC effect in a nonlinear QCD evolution equation. Through the numerical solutions of this evolution equation, we find that the random evolution of gluons in the transverse momentum space generates the Lipatov-singularity both in the linear and nonlinear terms. After regularization of these singularities according to the standard quantum field theory, the equation emerges a special nonlinear structure, which causes the chaotic oscillations and then generates the strong net antishadowing effect. Due to the restriction of the local momentum conservation, the antishadowing effect gathers the shadowed gluons to a state at a critical momentum, and forms the gluon condensate. We estimate the parameters in the GC solution, which predict that the hadron collisions $p - Pb$ and $Pb - Pb$ in the LHC are already close to the energy region of the GC effect. Since the huge number of gluons are condensed in a critical momentum, it should greatly increase the hadron cross section and release strong gamma-rays. We warn that further increase of the hadron collision energies in the next LHC plans may lead to unexpectedly intense gamma-rays in the accelerator, they look like the artificial mini GRBs and may damage the detectors.

Acknowledgments: This work is supported by the National Natural Science of China (No.11851303). Q.H. Chen acknowledges support from the National Natural Science of China (No.12147208).

References

- [1] V.N. Gribov, L.N. Lipatov, Sov. J. Nucl. Phys. 15 (1972) 438;
Yu.L. Dokshitzer, Sov. Phys. JETP. 46 (1977) 641;
G. Altarelli, G. Parisi, Nucl. Phys. B 126 (1977) 298.
- [2] L. N, Lipatov, Sov. J. Nucl. Phys. 23 (1976) 338;
V. S. Fadin, E.A. Kuraev, L. N. Lipatov, Phys. Lett. B60 (1975) 50;
E. A. Kuraev, L.N. Lipatov, V. S. Fadin, Sov. Phys. JETP. 44 (1976) 443;
E. A. Kuraev, L.N. Lipatov, V. S. Fadin, Sov. Phys. JETP. 45 (1977) 199;
I.I. Balitsky, L.N. Lipatov, Sov. J. Nucl. Phys. 28 (1978) 822.
- [3] L.V. Gribov, E.M. Levin, M.G. Ryskin, Phys. Rept. 100 (1983) 1;
A.H. Mueller, J.W. Qiu, Nucl. Phys. B 268 (1986) 427.
- [4] W. Zhu, Nucl. Phys. B 551(1999) 245;
W. Zhu, J.H. Ruan, Nucl. Phys. B 559 (1999) 378;
W. Zhu, Z.Q. Shen, HEP. & NP. 29 (2005) 109.
- [5] W. Zhu, Z.Q. Shen, J.H. Ruan, Chin. Phys. Lett. 25 (2008) 3605;
W. Zhu, Z.Q. Shen, J.H. Ruan, Nucl. Phys. B 911 (2016) 1;
W. Zhu, J.S. Lan, Nucl. Phys. B916 (2017) 647.
- [6] W. Zhu, J.S. Lan, J.H. Ruan, Int. J. Mod. Physics. E 27 (2018) 1850073.
- [7] F. Feng, J.H. Ruan, F. Wang, W. Zhu, Astrophys. J. 868 (2018) 2;
W. Zhu, P. Liu, J.H. Ruan, L. Feng, F. Wang, Astrophys. J. 896 (2020) 106;
W. Zhu, Z.C. Zheng, P. Liu, L.H. Wan, J.H. Ruan, F. Wang, JCAP. 01 (2021) 038;
J.H. Ruan, Z.C. Zheng, W. Zhu, JCAP. 08 (2021) 065.

- [8] W. Zhu, P. Liu, J.H. Ruan, F. Wang, *Astrophys. J.* 889 (2020) 127.
- [9] W. Zhu, P. Liu, J.H. Ruan, R.Q. Wang, F. Wang, *JCAP*, 09 (2020) 011.
- [10] I. Balitsky, *Nucl. Phys., B* 463 (1996) 99;
 Yu. Kovchegov, *Phys. Rev. D* 60 (1999) 034008;
 Yu. Kovchegov, *Phys. Rev. D* 61 (2000) 074018.
- [11] K. Golec-Biernat, M. Wüsthoff, *Phys. Rev. D* 59 (1998) 014017;
 K. Golec-Biernat, M. Wüsthoff, *Phys. Rev. D* 59 (1998) 014017.
- [12] D. Kharzeev, E. Levin, *Phys. Lett. B* 523 (2001) 79.
- [13] L.D. McLerran, R. Venugopalan, *Phys. Rev. D* 49 (1994) 2233;
 L.D. McLerran, R. Venugopalan, *Phys. Rev. D* 49 (1994) 3352;
 L.D. McLerran, R. Venugopalan, *Phys. Rev. D* 50 (1994) 2225.
- [14] A.J. Askew, J. Kwiecinski, A.D. Martin, P.J. Sutton, *Phys. Rev. D* 49 (1994) 4402.
- [15] C. Marquet, G. Soyez, *Nucl. Phys. A* 760 (2005) 208.
- [16] J.H. Ruan, Z.Q. Shen, J.F. Yang, W. Zhu, *Nucl. Phys. B* 760 (2007) 128.
- [17] M. Aaneodo, *Phys. Rep.* 240 (1994) 301.
- [18] Y.V. Kovchegov and E. Levin, *Quantum chromodynamics at high energy*, (2012)
 Cambridge university press.
- [19] V. Mathieu, *PoS FACESQCD2010*, 002 (2010) arXiv:hep=ph/1102.3875;
 L. Chang, C. Mezrag, H. Moutarde, C.D. Roberts, J. Rodriguez-Quintero, P.C. Tandy,
Phys. Lett. B 737 (2014) 23;
 C. D. Roberts, Insights into the Origin of Mass, Summary of a plenary presentation at "INPC 2019 - 27th International Nuclear Physics Conference", Glasgow, UK,

- 2019, arXiv:hep-ph/1909.12832;
- J. R. Quintero, L. Chang, K. Raya, C. D. Roberts, INPC 2019 proceedings, arXiv:hep-ph/1909.13802.
- [20] F.A. Aharonian, Very high energy cosmic gamma radiation: a crucial window on the extreme universe, World Scientific, 2004.
- [21] R. U. Abbasi, M. Abe, T. Abu-Zayyad, Phys. Rev. D 92 (2015) 032007.
- [22] R. Abdul Khalek, et al., Science Requirements and Detector Concepts for the Electron-Ion Collider, (EIC Yellow Report), (2021) BNL-220990-2021-FORE, JLAB-PHY-21-3198, LA-UR-21-20953.
- [23] P. Agostini¹, et al., (LHeC and FCC-he Study Group) arXiv:hep-ph/2007.14491.
- [24] C.D. Roberts, arXiv:hep-ph/1909.12832.